



WICHITA STATE  
UNIVERSITY

UNIVERSITY LIBRARIES

**Integrated micro x-ray tomography and  
pore-scale simulations for accurate  
permeability predictions of porous media**

Item Type	Article
Authors	Wang, Fangzhou;Riley, Gennifer A.;Egbo, Munonyedi Kelvin;Derby, Melanie M.;Hwang, Gisuk;Li, Xianglin
Citation	Fangzhou Wang, Gennifer A. Riley, Munonyedi Egbo, Melanie M. Derby, Gisuk Hwang, Xianglin Li. 2020. Integrated micro x-ray tomography and pore-scale simulations for accurate permeability predictions of porous media. <i>Frontiers in Heat and Mass Transfer</i> . vol. 15:art. no. 1:pp 1-8
Publisher	Global Digital Central
Download date	2026-05-19 01:05:58
Link to Item	<a href="https://doi.org/10.5098/hmt.15.1">https://doi.org/10.5098/hmt.15.1</a>



# INTEGRATED MICRO X-RAY TOMOGRAPHY AND PORE-SCALE SIMULATIONS FOR ACCURATE PERMEABILITY PREDICTIONS OF POROUS MEDIA

Fangzhou Wang<sup>a\*</sup>, Gennifer A. Riley<sup>b</sup>, Munonyedi Egbo<sup>c</sup>, Melanie M. Derby<sup>b</sup>, Gisuk Hwang<sup>c</sup>, Xianglin Li<sup>a†</sup>

<sup>a</sup> Department of Mechanical Engineering, University of Kansas, Lawrence, Kansas 66045, USA

<sup>b</sup> Department of Mechanical and Nuclear Engineering, Kansas State University, Manhattan, KS, 66506, USA

<sup>c</sup> Department of Mechanical Engineering, Wichita State University, Wichita, KS 67260, USA

## ABSTRACT

This study conducts pore-scale simulations and experiments to estimate the permeability of two different types of porous materials: metal foams and sintered copper particles with porosities of approximately 0.9 and 0.4, respectively. The integration of micro X-ray computed tomography with pore-scale computational fluid dynamics simulations develops a unique tool to capture the pore-scale geometry of porous media and accurately predict non-isotropic permeability of porous media. The pore-scale simulation not only results in improved prediction accuracy but also has the capability to capture non-isotropic properties of heterogeneous materials, which is a huge challenge for empirical correlations, volume averaged simulations, and simulations with simplified pore geometries. The permeability of air flow through 10-, 20- and 40-ppi aluminum foams (i.e., pore sizes of 2.54 mm, 1.27 mm, and 0.64 mm) are estimated to be  $8.25 \times 10^{-8} \text{ m}^2$ ,  $3.16 \times 10^{-8}$  and  $2.70 \times 10^{-8} \text{ m}^2$ , respectively. Experimental measurements and pore-scale simulations estimated permeabilities of water to be  $4.63 \times 10^{-11}$  and  $5.95 \times 10^{-11} \text{ m}^2$ , respectively, in a customized porous structure sintered from 200- $\mu\text{m}$  copper particles. The pore-scale models, validated by experimental data, were applied to simulate anisotropic properties of the material along three orthogonal directions. The estimated permeabilities of the 10-ppi (pore size of 2.54 mm) aluminum foam are  $8.2 \times 10^{-8}$ ,  $9.1 \times 10^{-8}$ , and  $1.1 \times 10^{-7} \text{ m}^2$  along the  $X$ ,  $Y$ , and  $Z$  directions, respectively. The estimated permeabilities of the sintered copper particles are  $5.95 \times 10^{-11}$ ,  $4.00 \times 10^{-11}$ , and  $5.78 \times 10^{-11} \text{ m}^2$  along the  $X$ ,  $Y$  and  $Z$  directions, respectively. The predicted properties of porous media can be applied to volume-averaged models and obtain better accuracy. This research also investigates the size of representative unit, which is critical to balance the accuracy and computational cost of simulations. Results recommend that for porous materials made from regular-shaped particles (e.g. spheres), the representative unit should be generally larger than three times of the particle or pore size if the flow is laminar.

**Keywords:** Metal Foams; Micro-CT; Permeability; CFD Simulation; Representative Unit.

## 1. INTRODUCTION

Various porous materials exist as natural substances and man-made porous materials are widely used in science, engineering, and industry because of their unique physical properties (Khaled and Vafai, 2003). Porous materials are characterized by their porosity (i.e., the void volume divided by the total volume). This study will experimentally measure and numerically simulate thermophysical properties of two manufactured porous materials that have very different porosities: metal foams and consolidated porous materials. Metal foams are porous metal structures that have extremely high porosity (e.g.,  $>0.9$ ) and low mass density, while exhibiting relatively high thermal and electric conductivity as well as strength. These unique properties make metal foams suitable for various energy applications. On the other hand, consolidated porous materials, which typically are manufactured from particles or powders using different sintering methods, have much lower porosity (e.g.,  $<0.5$ ). For example, parts produced from many additive manufacturing techniques are consolidated porous materials. While the advance of additive manufacturing technology provides great flexibility to produce customized geometries, accurate predictions of material properties are critical to the proper designs and customizations of functional parts based on the specific application needs.

Effective properties of porous materials – including metal foams and consolidated porous structures – such as thermal and electric conductivity, material strength, permeability, etc. are governed by not only properties of the solid matrix but also the pore-scale geometry, pore size, porosity, as well as connectivity of the solid and void. Many existing analyses and simulations apply empirical correlations to approximate effective properties of porous materials: Bruggeman correlation for tortuosity (Tjaden et al., 2016); Kozeny-Carman equation for permeability of laminar flow (Childs, Collis-George, and Ingram, 1950); Leverett J-function for capillary pressure of water saturation (Leverett, 1941); and various analytical and empirical correlations for stagnant thermal conductivity (Wang and Li, 2017). Empirical correlations are typically derived based on simplified pore or grain geometry and apply to limited pore size, pore geometry, and porosity. Improper use of empirical correlations could lead to orders of magnitudes of difference in predicted material properties (Flückiger et al., 2008; Andisheh-Tadbir et al., 2015; Li, Huang, and Faghri, 2016; Borup and Weber, 2019).

Computational fluid dynamics (CFD) simulations are a powerful tool to evaluate material properties and fluid flows through the porous materials. Both volume-averaged (i.e., continuous) models and pore-scale simulations have been applied to various applications of porous materials and provide valuable instructions for the device-level or system-level designs (Koito, 2019). Continuous models that simulate

\* Current Address: School of New Energy, Harbin Institute of Technology at Weihai, 2, Wenhua Road, Weihai, 264209, P.R. China

† Corresponding author: [xianglinli@ku.edu](mailto:xianglinli@ku.edu).

heat, mass, and electric transfer within porous media use effective parameters of porous materials, calculated from empirical correlations or experimental data, to simulate the overall properties and performance of the material/device. The accuracy of the results, however, are highly dependent on the accuracy of the effective parameters used in governing equations and boundary conditions (Yang et al., 2018; Abdulkadhim, Abed, and Al-Farhany, 2018). Pore-scale simulations that consider the exact tomography of porous materials are necessary to validate empirical correlations and provide accurate effective properties for continuous models (macroscopic models) (Chen et al., 2015). The accurate prediction of effective parameters of porous materials are important to simulate the thermal response, electrochemical performance, as well as electrical performance of devices made from porous materials.

Different techniques have been used measure or simulate the pore-scale tomography of porous structures: numerical reconstruction (Yeong and Torquato, 1998); Focused Ion Beam (FIB) - Scanning Electron Microscopy (SEM) (Saif et al., 2017); and X-ray Computed Tomography (Micro-CT) (Nickerson et al., 2019). The numerical reconstruction approach derives 3D geometrical structures from 2D images or purely computational simulations. It does not require advanced imaging technologies (e.g., Micro-CT or FIB-SEM) and has the flexibility to generate structures with different resolutions and sizes. Hao and Cheng numerically derived a porous fuel cell gas diffusion layer (GDL) based on the stochastic generation method (Hao and Cheng, 2010). Chen et al. reconstructed  $1.25\mu\text{m}\times 0.5\mu\text{m}\times 0.5\mu\text{m}$  3D nanostructures of shales using Markov chain Monte Carlo (MCMC) based on SEM images of shale samples (Chen et al., 2015). The reconstructed carbon paper with fiber structures (i.e., 0.79 porosity and  $7.5\mu\text{m}$  diameter) or the porous shale structures were then integrated into models to simulate intrinsic and relative permeability as well as diffusivity using the Lattice Boltzmann Method (LBM). The porous GDL with a given porosity and fiber diameter was numerically derived. The correlation function method derives correlation functions from measured 2D images as the target function (Yeong and Torquato, 1998; Jiao, Stillinger, and Torquato, 2007). Wang and Li applied the correlation function approach to numerically reconstruct 3D porous structures of electrodes of Li-O<sub>2</sub> battery from 2D SEM images (Wang and Li, 2018). The 3D digital electrodes were reconstructed iteratively to meet the target function in all three orthogonal directions (Kim and Pitsch, 2009; Blunt et al., 2013; Lopez-Haro et al., 2014). The process initialized with a trial 3D structure with a fraction of voxels as the matrix phase. The fraction of matrix voxels in the 3D structure equaled the volume fraction of matrix phase in 2D images. At each simulation step, a randomly selected matrix voxel was moved to an unoccupied void voxel so the volume fraction of each phase remained unchanged after the iteration. The energy of the 3D structure, which is equivalent to the difference between the current correlation function and the target function, was compared before and after the move to determine whether the new trial structure should be accepted or not. The reconstruction was considered complete if the energy of the 3D structure was smaller than the specified tolerance (e.g.  $10^{-6}$ ). Krishnan et al. numerically created a body-centered-cubic (BCC) structure (Krishnan, Murthy, and Garimella, 2006), which is similar to Kelvin's tetrakaidecahedron unit cell, as the representative unit of the open foam. The unstructured volume mesh of the numerically created structure was generated and use for further CFD simulations with commercial software (i.e., GAMBIT and FLUENT).

Many numerical reconstruction approaches simplified geometries due to computer algorithm or computational resource limitations. In addition, the sensitivity analysis of the reconstructed geometry on the simulations is often overlooked. Although simulations based on reconstructed geometries can obtain pore-scale simulation results, accuracy of simulation results are highly dependent on the representative geometry used for the simulation. Since material properties between the metal matrix and the filling fluid (air, water, etc.) are significantly different, accurate predictions of effective properties such as thermal and

electric conductivity, permeability, tensile and compression strength of porous media requires clear understanding on the connectivity of each phase. Simplifications of the pore geometry could lead to significant errors on predicted material properties. The FIB-SEM approach can measure 2D images of porous structures with high-resolutions and stacks of the 2D images could derive 3D pore-scale geometries of porous materials. However, the FIB-SEM approach is extremely time consuming and this approach is destructive. This approach is appropriate when characteristic pore sizes in the range of 1-10 nm are needed to reconstruct microstructures of very small samples such as electrodes of fuel cells or oil shale (Wargo et al., 2012).

The main advantage of the micro-CT approach is non-destructive and could be applied to reconstruct time-variations of 3D geometries of porous media *in situ*. This approach has been successfully applied to reconstruct 3D geometries of aluminum foams with different pore sizes in a previous study of the effective thermal conductivity of foam materials (Bodla, Murthy, and Garimella, 2010; Wang and Li, 2017). In addition, with the advance of additive manufacturing technology, the integration of micro-CT with 3D printing creates new avenue to design and produce new materials, structures, and templates (Zhang et al., 2018).

The objective of this study is to integrate high-resolution ( $\sim\mu\text{m}$ ) geometries of porous media obtained from micro-CT images with pore-scale CFD simulations to accurately predict intrinsic permeability of porous media, by considering detailed pore geometries and pore connectivity. This approach utilizes a tomographic X-ray microscope to measure and reconstruct 3D geometries of commercial metal foams as well as customized porous structures sintered from copper particles. Detailed pore-scale geometries will be applied to pore-scale CFD models without simplifications to elucidate anisotropic properties of porous materials by considering pore morphology, pore size and porosity as well as connectedness of the solid matrix and the filling fluid. Simulation results will be validated by property data reported by the material manufacturer and experimental data measured in this study. The understanding of pore-scale transport phenomena in porous media, through integration of micro-CT technology with pore-scale simulations, enables accurate predictions of material properties and design and optimization of porous media with complex geometries in various science and engineering applications.

## 2. WICK MANUFACTURING AND EXPERIMENTAL APPARATUSES

Porous copper structures were sintered using 200- $\mu\text{m}$ -diameter copper particles (section 2.1). Subsequently, permeability was measured in these structures (section 2.2) and three-dimensional geometries were generated using micro-CT for these porous copper structures and commercial aluminum foams with 10, 20, and 40 points per inch (section 2.3).

### 2.1 Fabrication of Sintered-Copper Particle Structures

A furnace sintering process was employed to fabricate a cylindrical wick within a 6.2-mm-inner diameter, 38-mm-long copper tube. For the wick structure, 200- $\mu\text{m}$ -diameter copper particles (Culox Technologies, Inc.) were used. The copper tube was secured vertically on a stainless-steel plate, while copper particles were poured into the copper tube as shown in Figure 1 (a) and (b). The copper-particle-filled tube was manually shaken to ensure that the copper particles were closely packed. Then, the tube was placed in a tube furnace [OTF-1200X MTI CORPORATION – see Figure 1 (b)] under 50 sccm inert gas (i.e., Argon) to prevent oxidation during the sintering process. The copper-particle-filled tube was kept in the furnace for three hours at 1,000°C, followed by natural cooling in the furnace at 5-10°C/min (temperature curve, Figure 2). After sintering, the copper-particle-filled tube was carefully removed from the tube furnace and stainless-steel plate were removed from the copper tube. The permeability and porosity were then measured, as discussed below.

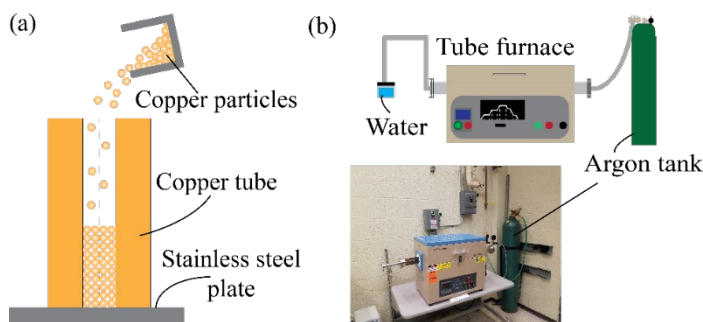


**Fig. 1** (a) Schematics of the fabrication process of a cylindrical wick structure, showing the copper particles being poured into the copper tube. (b) Schematic and actual images of the tube furnace used in the sintering process.

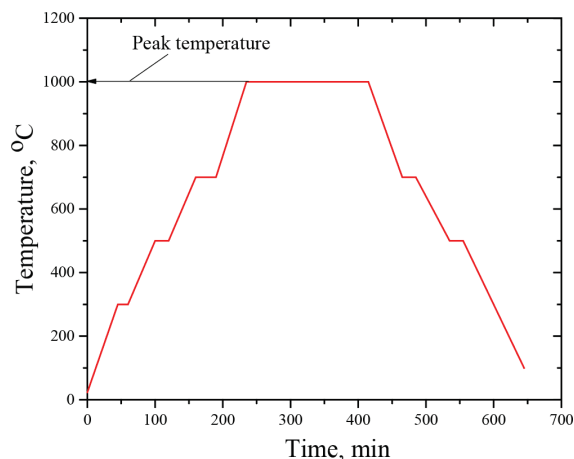


**Fig. 2** The sintering temperature as a function of the sintering time, including the maximum sintering temperature.

## 2.2 Permeability Measurements of Porous Structures

A closed-loop adiabatic experimental apparatus was used to measure the permeability of the porous structures (Figure 3). Water was pumped by a constant temperature water bath (Neslab, RTE-111) through the system loop, and its mass flow rate was measured by a Coriolis flowmeter (CMFS015M, Micro Motion) with an accuracy of  $\pm 0.05\%$  reading. Prior to the test section, flow developed in a plain copper 6.2 mm inner-diameter, 203 mm-long developing length. The test section was a 6.2-mm-inner-diameter, 38-mm-long copper pipe with the sintered copper structure described in section 2.1. After the test section was a 38-mm exit length comprised of plain, copper tubing. The temperature of the water was measured by type T thermocouples ( $\pm 0.2^\circ\text{C}$ ) at the start of the test section and the end of the exit length and pressure drops were measured across the same region using a 100-psi pressure transducer (Setra Model 230) with  $\pm 0.25\%$  full scale accuracy ( $\pm 1.72\text{ kPa}$ ). A modified experimental apparatus with a 914-mm developing length and 203-mm exit length was used to verify that the flow was fully developed and two testing configurations were comparable. Data were collected at mass flow rates from 0.002 kg/s to 0.009 kg/s in increments of 0.001 kg/s. For a given flow rate, the mass flow rate, temperature and pressure drop were averaged over a 60-second period once the flow rate is stable.

## 2.3 Micro-Tomography and Reconstruction of 3D Geometries

Micro-CT of porous structures [commercial aluminum foams with 10, 20, and 40 points per inch (ppi) from ERG Aerospace Corporation and customized copper cylinder from 200  $\mu\text{m}$  particles] were obtained using Xradia MicroXCT-400 Tomographic X-Ray Microscope. All measurements were taken at 0.5 times magnification with the spatial resolution of 14  $\mu\text{m}$ . Slices of X-ray images of samples were measured

every  $1^\circ$  and reconstructed after the sample rotated  $180^\circ$ . The micro-tomography was saved as stacks of 2D gray-scale images and each voxel had a gray-scale value between 0 and 255. The value of each voxel depends on the X-ray absorptions rate, therefore, value indicated whether the voxel is solid matrix or void.

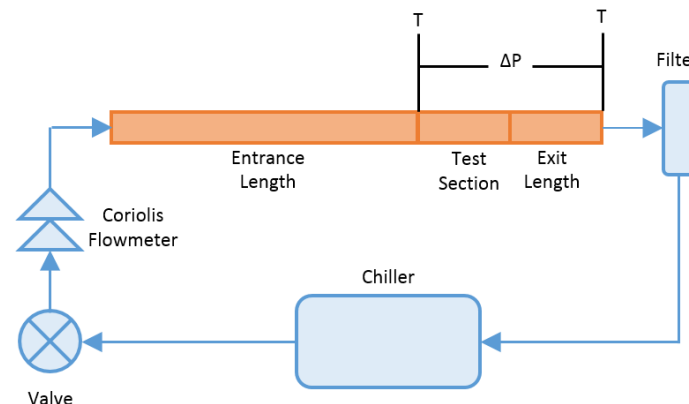


**Fig. 3** The experimental apparatus to measure the permeability of the porous structures.

## 3. MODEL SIMULATIONS

### 3.1 Image Processing

Each voxel of the measured micro-tomography has a different intensity depending on the X-ray absorption rate of the material. The gray scale value (between 0 and 255) of each voxel, relative to a given threshold value, differentiates between solid materials or voids. This study used the threshold value approach to convert the gray scale images to binary images (i.e., 0-1) and reconstructed the solid matrices and voids of porous materials. It should be noted that the large data size of reconstructed 3D micro-tomography (i.e.,  $1000 \times 1000 \times 1000$  voxels) makes it very time consuming to generate meshes and carry out further CFD simulations. Therefore, this study trimmed a fraction (i.e., as large as  $500 \times 800 \times 600$  voxels) of the whole micro-tomography structure to balance between computational time and the representativeness of the simulated geometry. Since defining a representative unit is critical and challenging for pore-scale simulations of porous media to provide accurate simulation with reasonable computational cost, this study also strategically trimmed the structure to investigate the smallest units that can represent the whole porous materials.

The 3D micro-tomography data was first sliced into a stack of 2D images. The stack of images were then processed by open-source image processing software ImageJ to a binary structure (i.e., solid matrix or void) based on the threshold value. Using the binary structure, open-source visualization software ParaView generates a surface mesh (.stl) for solid and void phases. The surface mesh is imported into StarCCM++ (version 13.04.011) to generate a high-quality volume mesh for CFD simulations of fluid flow within the porous material.

Additional image processing was needed for porous structures sintered from copper particles due to isolated holes inside the copper particles, as seen in the micro-tomography (Figure 4a). These isolated holes are from the supplied copper particles and most of them stay isolated in finished parts. Since these dead holes are not accessible to the fluid and do not contribute to the effective porosity and permeability of the sintered structure, all these isolated holes were filled using an available algorithm “Fill Holes” in ImageJ before the CFD simulation (Fig. 4b). Figure 5 shows the processed structures of the solid matrix and void for 20-ppi (pore size of 1.27 mm) aluminum foam and structure sintered from 200  $\mu\text{m}$  copper particles. The processed and cropped images were then saved as .stl files using ParaView to be further processed by CFD simulations using StarCCM++, as described previously.

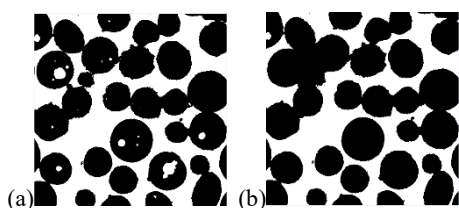


**Fig. 4** Binary images of a slice of micro-tomography of sintered copper: (a) before and (b) after filling dead holes. The physical size of the slices are 1.61 mm×1.61 mm.

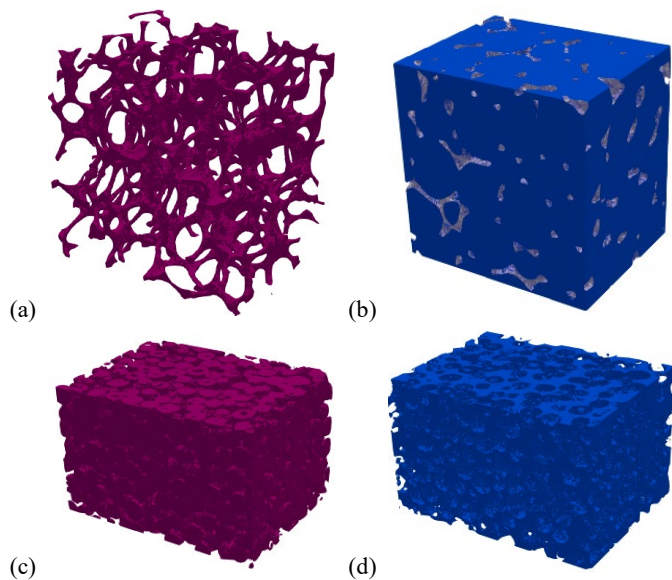


**Fig. 5** Micro-tomography of aluminum foam with 1.27 mm pore size (9.4 mm×9.4 mm×7.5 mm): (a) aluminum and (b) void; micro-tomography of sintered copper structure (2.57 mm×1.93 mm×1.61 mm): (c) copper and (d) void.

### 3.2 Model Setup and Boundary Conditions

The CFD simulations were conducted based on reconstructed micro-tomography geometry. The objective file (.stl) of the tomography was imported into StarCCM++ for steady state simulations under constant temperature. To simulate permeability, the void phase was imported as a part and considered as the computational domain. The governing equations that were solved in this study include:

Continuity equation:

$$\nabla \cdot (\rho \vec{u}) = 0 \quad (1)$$

Momentum equation:

$$\nabla \cdot (\rho \vec{u} \vec{u}) = -\nabla p + \mu \nabla^2 \vec{u} + \rho \vec{g} \quad (2)$$

where  $\rho$  is the density of the fluid,  $\vec{u}$  is the velocity,  $p$  is the pressure,  $\mu$  is the viscosity, and  $\vec{g}$  is the gravitational acceleration. This study used both air and water as working fluid to validate the simulated pressure gradients at distinct mass flow rates using reported data and experimental results. In the sintered 200- $\mu$ m copper structure, Reynolds numbers for water and air are 30.8 and 20.4, respectively, at water velocities of 1 m/s and air velocities of 10 m/s. It should be noted that the pore size for the  $Re$  number is estimated from the particle size (Beltrán et al., 2019):

$$Re = \frac{\rho u d_{\text{pore}}}{\mu} = \frac{\rho u d_{\text{particle}}/6.46}{\mu} \quad (3)$$

The calculated  $Re$  number indicates that the flow is generally laminar when the water velocity is less than 1 m/s and the air velocity is less than 10 m/s (i.e., Darcy flow or inertial flow) according to the regimes of porous media flows categorized by Dybbs and Edwards (Dybbs and Edwards, 1984). Therefore, the current study used the default parameters

and constants of laminar flow at steady state in StarCCM++. After importing the simulated void structure, six artificial blocks were added next to the six faces of the imported part. Then six boundaries (top, bottom, left, right, front, and back) were created by imprinting surfaces between the imported part and the six added blocks. Given inlet fluid velocity and fully-developed pressure outlet boundary conditions were applied respectively to the direction of the simulated permeability. All other four boundaries as well as the void/solid interface were set as non-permeable walls.

It should be mentioned that the experiments controlled and measured total mass flow rates of the fluid and calculated the superficial velocity based on the density of the fluid and cross-sectional area of the sample. Therefore, the velocity at the inlet of the computational domain ( $u$ ) set as the boundary condition, needs to be converted into superficial velocity ( $u_s$ ) using porosity at the inlet boundary ( $\epsilon$ ) in order to compare with the experimental results:

$$u_s = \epsilon u \quad (4)$$

where the inlet porosity, which is the volume fraction of void on the total surface, is determined using the histogram of voxel values from the following slices (Figure 6). The calculated surface porosities are 0.40, 0.38, and 0.33 for  $x$ -,  $y$ -,  $z$ -planes of the sintered copper structure, respectively, and approximately 0.93 for all planes of aluminum foams.

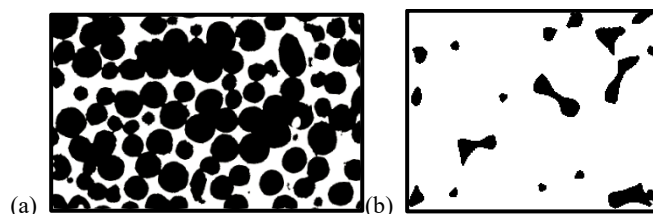


**Fig. 6** Distributions of solid (black) and void (white) at the inlets of the sintered (a) copper structure (2.57 mm×1.61 mm) and (b) aluminum foam (9.4 mm×7.5 mm).

### 3.3 Grid-Independence

The physical size of the simulated geometry is 2.57 mm×1.93 mm×1.61 mm. The mesh independence study was carried out by adjusting the base mesh size between 50 and 5  $\mu$ m, which result in 1,020,878 to 13,406,768 mesh elements, and simulating the pressure drop of water flow through sintered porous copper structure at 0.3 m/s inlet velocity (or 0.12 m/s superficial velocity). Results based on the mesh shown in Figure 7 (a) indicate that the change of simulation results are less than 1% when the base size is set as 25  $\mu$ m (2,117,892 mesh) or smaller. Considering the accuracy and computational cost, this study used the “polyhedral” meshes and the base size of 25  $\mu$ m.

### 3.4 Model Validations Using Duocel® Aluminum Foams

ERG Materials & Aerospace reports the measured pressure drop of air through Duocel® aluminum foams with 2.54 mm, 1.27 mm, and 0.64 mm pore sizes<sup>3</sup>. The model simulations of pressure drop at various air velocities are compared with reported data in Figure 7 (b) to validate the model and the pore-scale simulation approach. Results in Figure 7 (b) indicate that the pore-scale simulations match very well with experimental data: the permeability of 10-ppi aluminum foam (pore size of 2.54 mm) estimated from experimental data and simulation results are  $8.32 \times 10^{-8}$  and  $8.25 \times 10^{-8}$  m<sup>2</sup>, respectively. Considering the fact that permeability can change by orders of magnitude after a very small change on pore-scale structure (Li, Huang, and Faghri, 2015), the simulation results match with experimental data extremely well. The permeability of aluminum foams with 1.27 mm (20-ppi) and 0.64 mm (40-ppi) pore sizes are estimated to be  $3.16 \times 10^{-8}$  and  $2.70 \times 10^{-8}$  m<sup>2</sup>, respectively, from the simulated pressure gradient data. As expected, the permeability slightly decreases with the decrease of the pore size.

<sup>3</sup> <http://ergaerospace.com/technical-data/duocel-foam-pressure-drop-charts/>

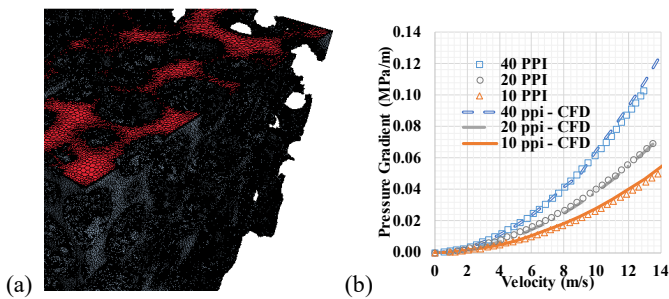


**Fig. 7** (a) Zoom-in volume mesh generated based on the micro-tomography and (b) simulated vs. reported pressure gradients at different air flow velocities using Duocel® aluminum foams with different pore sizes: 2.54 mm (10 ppi), 1.27 mm (20 ppi), and 0.64 mm (40 ppi).

#### 4. RESULTS AND DISCUSSION

After validating the pore-scale simulations using ERG’s reported pressure gradient vs. air flow rate data, this study develops similar pore-scale simulation approach for customized porous structures made by sintering 200- $\mu\text{m}$ -diameter copper particles.

##### 4.1 Applications of the Model to Sintered Copper Structures

The pressure drop experiments discussed in section 2.2 generated consistent results (Figure 8). Pressure drops with the 203-mm and 914-mm developing sections before the testing sample were nearly identical. The pressure drops and superficial velocities reported in Figure 8 were used to fit the permeability,  $K$ , as well as the inertial coefficient,  $F$ , of the porous media (Leong and Jin, 2006):

$$\frac{\Delta p}{L} = \frac{\mu}{K} \vec{V} + \rho \frac{F}{\sqrt{K}} \vec{V}^2 \quad (5)$$

where  $\mu$  and  $\rho$  are the viscosity and density of the fluid and  $L$  is the geometry of the porous media. The derived permeability by curve fitting the experimental data in Figure 8 is  $4.6 \times 10^{-11} \text{ m}^2$ . The permeability of the porous media can be estimated by the Carman-Kozeny equation (Childs, Collis-George, and Ingram, 1950):

$$\frac{K}{d^2} = \frac{1}{180} \frac{\varepsilon^3}{(1-\varepsilon)^2} \quad (6)$$

where  $d$  is the average pore size (i.e., 200  $\mu\text{m}$ ), and  $\varepsilon$  is the porosity of the porous media. The permeability estimated by the Carman-Kozeny equation ( $3.98 \times 10^{-11} \text{ m}^2$ ) is similar to the fitted permeability based on the pressure gradient data. The data fitting based on pressure gradient vs. fluid velocity is a reasonable approach to estimate the permeability of porous media. The similar curve-fitting approach will be used to estimate permeability of porous materials using simulated data.

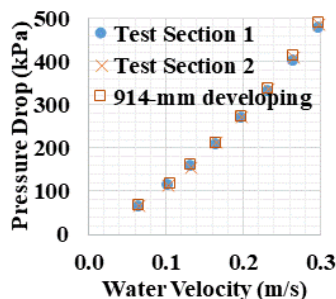


**Fig. 8** Experimental data of pressure drop at different water flow velocities for two different sintered copper test sections with a 203-mm developing length, as well as experiments with a 914-mm developing length.

##### 4.2 Non-Isotropic Properties

Experimental pressure drop and mass flow data in the sintered copper structure are also used to validate model simulations of pressure gradients as shown in Figure 9 (a). The pore-scale model results agree very well with experimental data, especially along the  $X$  direction. From simulations, the permeability of the sintered copper structure to water is

estimated to be  $5.95 \times 10^{-11}$ ,  $4.00 \times 10^{-11}$ , and  $5.78 \times 10^{-11} \text{ m}^2$  along the  $X$ ,  $Y$ , and  $Z$  directions, respectively. Because of the asymmetric characteristic geometry, porous materials are generally non-isotropic materials with different properties in different directions. As a result, the pressure gradients and the resulting permeability of the sintered structure are non-isotropic.

Similarly, commercial aluminum foams have non-isotropic properties as well. Figure 9 (b) compares the reported pressure gradients of air by ERG and the simulated pressure gradients of air along through orthogonal directions of a 10-ppi aluminum foam (pore size of 2.54 mm). The estimated permeability from experimental data is  $8.3 \times 10^{-8} \text{ m}^2$  and the estimated permeabilities from model simulations are  $8.2 \times 10^{-8}$ ,  $9.1 \times 10^{-8}$ , and  $1.1 \times 10^{-7} \text{ m}^2$  along the  $X$ ,  $Y$ , and  $Z$  directions, respectively. The averaged permeability obtained from simulations ( $9.3 \pm 1.2 \times 10^{-8} \text{ m}^2$ ) is close to the estimated permeability from experimental data ( $8.25 \times 10^{-8} \text{ m}^2$ ).

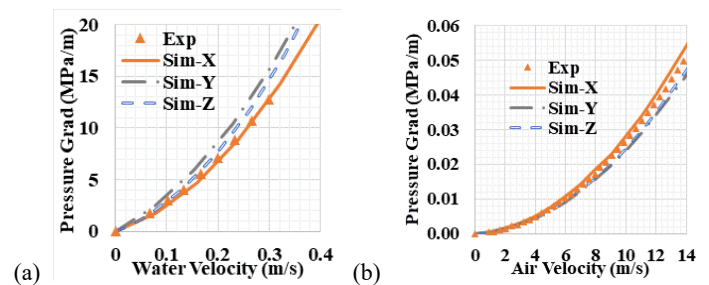


**Fig. 9** Pressure gradients of (a) water flow through the sintered copper structure and (b) air flow through the 10-ppi aluminum foam (pore size of 2.54 mm) along three orthogonal directions.

##### 4.3 Size of the Representative Unit

One of the biggest challenges in CFD simulations of porous media is to determine the dimensions of the representative unit for accurate simulations with limited computational cost. Although a large model domain is preferred to represent the whole porous media, large representative units require more computational resources and the size of model geometry can be limited by available tomography data. Therefore, the balance between computational time and accuracy is critical to simulate properties of porous media. As a result, this study trims micro tomography data into different sizes (i.e., 200, 400, and 800 voxels along the flow direction) as the computational domain. The investigations with different sample sizes provide criteria to determine representative units of porous materials.

The entrance length for laminar and turbulent flows can be estimated using the following empirical correlation:

$$\frac{L_{\text{entrance}}}{d_{\text{particle}}} = \begin{cases} 0.06 Re & \text{Laminar} \\ 4.4 Re^{1/6} & \text{Turbulent} \end{cases} \quad (7)$$

where  $d_{\text{particle}}$  is the characteristic dimension (particle size) and  $L_{\text{entrance}}$  is the entrance length of the flow. The length of the representative unit of the porous media  $L$  has to be much longer than the entrance length. Based on the calculated  $Re$  numbers for the water flow, 30.8, the entrance length of the water flow at 1 m/s intrinsic velocity ( $\sim 0.4 \text{ m/s}$  superficial velocity for sintered copper structure) is about 1.8 times the particle size of the sintered copper material. Similarly, the entrance length of the air flow at 10 m/s intrinsic velocity ( $\sim 9.3 \text{ m/s}$  superficial velocity for aluminum foam) is about 1.2 times the pore size of aluminum foams. To validate this analysis, the local pressure distribution and averaged pressure drops along the flow direction at  $Y=1/2$  and  $Z=1/2$  planes are plotted at the water flow rate of 0.05 m/s (Figure 10). The pressure drops almost linearly along the flow direction when the flow is a few layers of copper particles within the sintered structure. Results are consistent with conclusions from Mu et al. (Mu, Sungkorn, and Toelke, 2016) that the size of the representative unit could be less than three times the particle size for porous media with regular shapes (e.g. made from spherical particles).

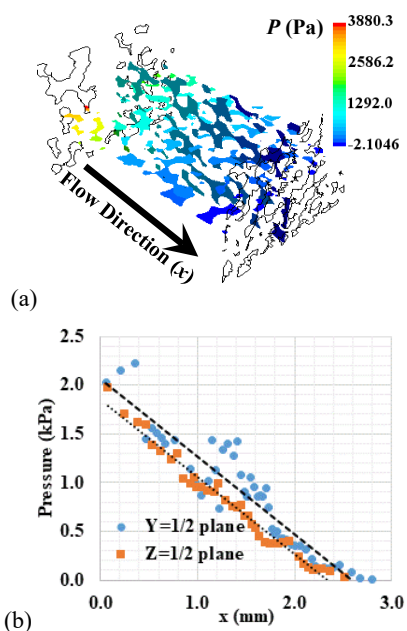


**Fig. 10** Model simulation of (a) pressure distributions on  $Y=1/2$  and  $Z=1/2$  planes and (b) averaged pressure changes along the flow direction ( $X$  direction).

To further understand the size of the representative unit and impact of the fully developed flow, this study compares the simulated pressure drops with different sizes of computational domain as shown in Figure 11: 2.57 mm (800 voxels), 1.29 mm (400 voxels), and 0.64 mm (200 voxels). The ratios between the sample and the copper particle diameters are 13.9, 6.4, and 3.2, respectively. For flows in porous media with  $Re$  numbers greater than about 1 to 10, inertial effects can also become significant. In order to derive the permeability from the linear correlation between pressure drop and flow velocity, the flow should be within the laminar flow without significant inertial effects. Therefore, the model simulates cases with water velocity less than 0.05 m/s, i.e.,  $Re \leq 1.5$ . The simulated pressure gradients of water flow at low flow rates as well as the fitted linear trend lines are compared in Figure 11 (b) to illustrate the pressure gradient simulated by representative units with different sizes. The simulated pressure gradients at various flow rates with 1.29 mm or larger computational domains are similar. But the pressure gradient predicted based on the 0.66-mm computational domain is noticeably higher likely due to the faster pressure drop in the developing flow region. Therefore, for porous media made from particles with regular shapes or metal foams with repeated open pore structures, the size of representative unit is recommended to be at least 3 times of the length scale (particle size or pore size).

### 5. CONCLUSIONS

Porous media are commonly used in energy applications due to their unique thermal physical properties including high surface area, low density, high thermal conductivity, low flow resistance, etc. This study conducts experiments and pore-scale simulations to accurately estimate the permeability of two different types of porous materials: metal foams with porosity close to 0.9 and sintered copper particles with porosity near 0.4. The integration of micro-CT images with pore-scale computational fluid dynamics simulations develops a unique tool to predict thermal physical properties of porous media. The experimental measurements and model simulation in this study lead to the following conclusions:

- The permeability of air flow through 10-, 20- and 40-ppi aluminum foams with pore sizes of 2.54 mm, 1.27 mm, and 0.64 mm are estimated to be  $8.25 \times 10^{-8}$  m<sup>2</sup>,  $3.16 \times 10^{-8}$  m<sup>2</sup> and  $2.70 \times 10^{-8}$  m<sup>2</sup>, respectively. Porous media with smaller pore size have higher flow resistance and result in lower permeability.

- The permeability of water flow through a customized porous structure sintered from 200- $\mu$ m copper particles estimated by experimental measurement and pore-scale simulations are  $4.63 \times 10^{-11}$  and  $5.95 \times 10^{-11}$  m<sup>2</sup>, respectively.
- Properties of porous media along different directions could be significantly different. The estimated permeability of the 10-ppi aluminum foam (pore size of 2.54 mm) are  $8.2 \times 10^{-8}$ ,  $9.1 \times 10^{-8}$ , and  $1.1 \times 10^{-7}$  m<sup>2</sup> along the  $X$ ,  $Y$ , and  $Z$  directions, respectively. The estimated permeability of the sintered copper particles are  $5.95 \times 10^{-11}$ ,  $4.00 \times 10^{-11}$ , and  $5.78 \times 10^{-11}$  m<sup>2</sup> along the  $X$ ,  $Y$  and  $Z$  directions, respectively.
- For porous materials made from spherical-shape particles, the representative unit should be generally larger than three times of the particle or pore size if the flow is in laminar flow region.

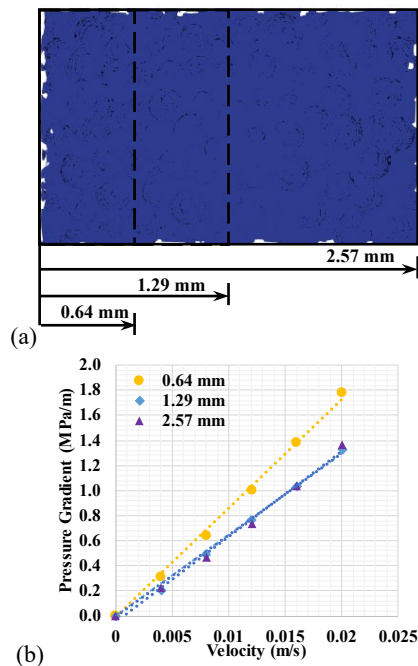


**Fig. 11** (a) Different sizes of computational domain as representative units of the simulation; (b) simulated pressure gradient of water flow across sintered copper with different sizes of computational domain.

### ACKNOWLEDGEMENTS

The authors gratefully acknowledge the financial support by NASA Cooperative Agreement Notice, Grant Number 80NSSC18M0030. Tomography data were obtained from the tomographic X-ray microscope at the Institute for Bioengineering Research (IBER) at the University of Kansas. F.W. and X.L. also want to acknowledge Dr. Charles Ye at IBER for providing training in the use of the tomographic X-ray microscope.

### REFERENCES

- Abdulkadhim, A., Azher A., and Khaled A., 2018, "Computational Investigation of Conjugate Heat Transfer in Cavity Filled with Saturated Porous Media," *Frontiers in Heat and Mass Transfer*, **11** (12). <https://dx.doi.org/10.5098/hmt.11.12>
- Andisheh-Tadbir, M., Hannach, M.E., Kjeang, E., and Bahrami, M., 2015. "An Analytical Relationship for Calculating the Effective Diffusivity of Micro-Porous Layers." *International Journal of Hydrogen Energy* **40** (32): 10242–50. <https://doi.org/10.1016/j.ijhydene.2015.06.067>.
- Beltrán, A., Hernández-Díaz, D., Chávez, O., García, A., Mena, B., and Zenit, R., 2019. "Experimental Study of the Effect of Wettability on the

Relative Permeability for Air–Water Flow through Porous Media.” *International Journal of Multiphase Flow* **120** (November): 103091.

<https://doi.org/10.1016/j.ijmultiphaseflow.2019.103091>.

Blunt, M.J., Bijeljic B., Dong, H., Gharbi, O., Iglauer, S., Mostaghimi, P., Paluszny, A., and Pentland, C., 2013. “Pore-Scale Imaging and Modelling.” *Advances in Water Resources*, 35th Year Anniversary Issue, 51 (January): 197–216.

<https://doi.org/10.1016/j.advwatres.2012.03.003>.

Bodla, K.K., Murthy, J.Y., and Garimella, S.V., 2010. “Microtomography-Based Simulation of Transport through Open-Cell Metal Foams.” *Numerical Heat Transfer, Part A: Applications* **58** (7): 527–44.

<https://doi.org/10.1080/10407782.2010.511987>.

Borup, R., and Weber, A., 2019. “FC135: FC-PAD: Fuel Cell Performance and Durability Consortium.” Presented at the 2019 Annual Merit Review Proceedings, Washington D.C., April 30.

[https://www.hydrogen.energy.gov/annual\\_review19\\_fuelcells.html#performance](https://www.hydrogen.energy.gov/annual_review19_fuelcells.html#performance).

Chen, L., Zhang L., Kang, Q., Viswanathan, H.S., Yao, J., and Tao, W., 2015. “Nanoscale Simulation of Shale Transport Properties Using the Lattice Boltzmann Method: Permeability and Diffusivity.” *Scientific Reports* **5** (1): 1–8.

<https://doi.org/10.1038/srep08089>.

Childs, E.C., Collis-George N., and Ingram, T.G., 1950. “The Permeability of Porous Materials.” *Proceedings of the Royal Society of London. Series A. Mathematical and Physical Sciences* **201** (1066): 392–405.

<https://doi.org/10.1098/rspa.1950.0068>.

Dybbbs, A., and Edwards, J., 1984. “A New Look at Porous Media Fluid Mechanics — Darcy to Turbulent.” *Fundamentals of Transport Phenomena in Porous Media*, **82**: 199–256.

[https://doi.org/10.1007/978-94-009-6175-3\\_4](https://doi.org/10.1007/978-94-009-6175-3_4)

Flückiger, R., Freunberger, S.A., Kramer, D., Wokaun, A., Scherer, G.G., and Büchi, F.N., 2008. “Anisotropic, Effective Diffusivity of Porous Gas Diffusion Layer Materials for PEFC.” *Electrochimica Acta* **54** (2): 551–59.

<https://doi.org/10.1016/j.electacta.2008.07.034>.

Hao, L., and Cheng, P., 2010. “Pore-Scale Simulations on Relative Permeabilities of Porous Media by Lattice Boltzmann Method.” *International Journal of Heat and Mass Transfer* **53** (9–10): 1908–13.

<https://doi.org/10.1016/j.ijheatmasstransfer.2009.12.066>.

Jiao, Y., Stillinger, F.H., and Torquato, S., 2007. “Modeling Heterogeneous Materials via Two-Point Correlation Functions: Basic Principles.” *Physical Review E* **76** (3): 031110.

<https://doi.org/10.1103/PhysRevE.76.031110>.

Khaled, A.R.A., and Vafai, K., 2003. “The Role of Porous Media in Modeling Flow and Heat Transfer in Biological Tissues.” *International Journal of Heat and Mass Transfer* **46** (26): 4989–5003.

[https://doi.org/10.1016/S0017-9310\(03\)00301-6](https://doi.org/10.1016/S0017-9310(03)00301-6).

Kim, S.H., and Pitsch, H., 2009. “Reconstruction and Effective Transport Properties of the Catalyst Layer in PEM Fuel Cells.” *Journal of The Electrochemical Society* **156** (6): B673–81.

<https://doi.org/10.1149/1.3106136>.

Koito, Y., 2019. “Numerical Analyses on Vapor Pressure Drop in a Centered-Wick Ultra-Thin Heat Pipe.” *Frontiers in Heat and Mass Transfer (FHMT)* **13** (26).

<http://dx.doi.org/10.5098/hmt.13.26>

Krishnan, S., Murthy, J.Y., and Garimella, S.V., 2006. “Direct Simulation of Transport in Open-Cell Metal Foam.” *Journal of Heat Transfer* **128** (8): 793–99.

<https://doi.org/10.1115/1.2227038>.

Leong, K. C., and Jin, L. W., 2006. “Effect of Oscillatory Frequency on Heat Transfer in Metal Foam Heat Sinks of Various Pore Densities.” *International Journal of Heat and Mass Transfer* **49** (3): 671–81.

<https://doi.org/10.1016/j.ijheatmasstransfer.2005.08.015>.

Leverett, M.C., 1941. “Capillary Behaviour in Porous Solids”, *Transactions of the AIME*, **142** (01): 159–72.

<https://doi.org/10.2118/941152-G>

Li, X., Huang, J., and Faghri, A., 2015. “Modeling Study of a Li-O<sub>2</sub> Battery with an Active Cathode.” *Energy* **81** (1): 489–500.

<https://doi.org/10.1016/j.energy.2014.12.062>

Li, X., Huang, J., and Faghri, A., 2016. “A Critical Review of Macroscopic Modeling Studies on Li O<sub>2</sub> and Li–Air Batteries Using Organic Electrolyte: Challenges and Opportunities.” *Journal of Power Sources* **332**: 420–46.

<https://doi.org/10.1016/j.jpowsour.2016.09.127>.

Lopez-Haro, M., Guétaz, L., Printemps, T., Morin, A., Escribano, S., Jouneau, P. H., Bayle-Guillemaud, P., Chandezon, F., and Gebel, G., 2014. “Three-Dimensional Analysis of Nafion Layers in Fuel Cell Electrodes.” *Nature Communications* **5**: 5229.

<https://doi.org/10.1038/ncomms6229>.

Mu, Y., Sungkorn, R., and Toelke, J., 2016. “Identifying the Representative Flow Unit for Capillary Dominated Two-Phase Flow in Porous Media Using Morphology-Based Pore-Scale Modeling.” *Advances in Water Resources*, **95**: 16–28.

<https://doi.org/10.1016/j.advwatres.2016.02.004>.

Nickerson, S., Shu, Y. Zhong, D., Könke, C., and Tandia, A., 2019. “Permeability of Porous Ceramics by X-Ray CT Image Analysis.” *Acta Materialia* **172**: 121–30.

<https://doi.org/10.1016/j.actamat.2019.04.053>.

Saif, T., Lin, Q., Butcher, A.R., Bijeljic, B., and Blunt, M.J., 2017. “Multi-Scale Multi-Dimensional Microstructure Imaging of Oil Shale Pyrolysis Using X-Ray Micro-Tomography, Automated Ultra-High Resolution SEM, MAPS Mineralogy and FIB-SEM.” *Applied Energy* **202**: 628–47.

<https://doi.org/10.1016/j.apenergy.2017.05.039>.

Tjaden, B., Cooper, S.J., Brett, D.J., Kramer, D. and Shearing, P.R., 2016. “On the Origin and Application of the Bruggeman Correlation for Analysing Transport Phenomena in Electrochemical Systems.” *Current Opinion in Chemical Engineering*, **12**: 44–51.

<https://doi.org/10.1016/j.coche.2016.02.006>.

Wang, F., and Li, X., 2017. “The Stagnant Thermal Conductivity of Porous Media Predicted by the Random Walk Theory.” *International Journal of Heat and Mass Transfer*, **107**: 520–33.

<https://doi.org/10.1016/j.ijheatmasstransfer.2016.11.069>

Wang, F., and Li, X., 2018. “Pore-Scale Simulations of Porous Electrodes of Li–O<sub>2</sub> Batteries at Different Saturation Levels.” *ACS Applied Materials & Interfaces* **10** (31): 26222–32.

<https://doi.org/10.1021/acsami.8b06624>.

Wargo, E. A., Hanna, A. C., Çeçen, A., Kalidindi, S.R., and Kumbur, E.C., 2012. “Selection of Representative Volume Elements for Pore-Scale Analysis of Transport in Fuel Cell Materials.” *Journal of Power Sources* **197**: 168–79.

<https://doi.org/10.1016/j.jpowsour.2011.09.035>.

Yang, X., Bai, Q., Guo, Z., Niu, Z., Yang, C., Jin, L., Lu, T., and Yan, J., 2018. “Comparison of Direct Numerical Simulation with Volume-Averaged Method on Composite Phase Change Materials for Thermal Energy Storage.” *Applied Energy* **229**: 700–714.

<https://doi.org/10.1016/j.apenergy.2018.08.012>.

Yeong, C.L.Y., and Torquato, S., 1998. "Reconstructing Random Media. II. Three-Dimensional Media from Two-Dimensional Cuts." *Physical Review E* **58** (1): 224–33.  
<https://doi.org/10.1103/PhysRevE.58.224>.

Zhang, X., Keramati, H., Arie, M., Singer, F., Tiwari, R., Shoostari, A. and Ohadi, M., 2018. "Recent Developments in High Temperature Heat Exchangers: A Review." *Frontiers in Heat and Mass Transfer* **11** (18).  
<https://doi.org/10.5098/hmt.11.18>.